Dalton Transactions

ROYAL SOCIETY OF CHEMISTRY

PAPER

View Article Online
View Journal | View Issue

Cite this: *Dalton Trans.*, 2024, **53**, 12917

Cyclometalated iridium(III) tetrazine complexes for mitochondria-targeted two-photon photodynamic therapy†

Zanru Tan,‡[a] Mingwei Lin,‡[a] Jiangping Liu,*[b] Huihui Wu*[c] and Hui Chao *[a,d]

Received 8th June 2024,
Accepted 12th July 2024

DOI: 10.1039/d4dt01665c

rsc.li/dalton

The fast-moving field of photodynamic therapy (PDT) has provided fresh opportunities to expand the potential of metallodrugs to combat cancers in a light-controlled manner. As such, in the present study, a series of cyclometalated Ir(III) complexes modified with a tetrazine functional group (namely, **Ir-ppy-Tz**, **Ir-pbt-Tz**, and **Ir-dfppy-Tz**) are developed as potential two-photon photodynamic anticancer agents. These complexes target mitochondria but exhibit low toxicity towards HLF primary lung fibroblast normal cells in the dark. When receiving a low-dose one- or two-photon PDT, they become highly potent towards A549 lung cancer cells (with IC_{50} values ranging from 24.0 nM to 96.0 nM) through the generation of reactive oxygen species (ROS) to induce mitochondrial damage and subsequent apoptosis. Our results indicated that the incorporation of tetrazine with cyclometalated Ir(III) matrices would increase the singlet oxygen ($^1O_2$) quantum yield (Φ_Δ) and, meanwhile, enable a type I PDT mechanism. **Ir-pbt-Tz**, with the largest two-photon absorption (TPA) cross-section (σ_2 = 102 GM), shows great promise in serving as a two-photon PDT agent for phototherapy.

Introduction

As a clinically approved therapeutic modality for treating various cancers, PDT has been increasingly favored in recent years due to its advantages of having a non-invasive nature and requiring minimal surgical intervention.[1,2] During PDT, the activation of PSs through light irradiation induces the generation of ROS, which instigate potent cytotoxicity in localized tumor cells.[3] Before a PS becomes clinically viable, a handful of major challenges must be tackled, including the potential toxicity incurred by the administration of an overdose of PS agents to guarantee efficacy,[4] and the limited penetration depth through tissues of UV-vis light corresponding to the absorption profile of many PSs.[5] Therefore, a promising PS should manifest near-infrared (NIR) absorption ability, high-performance photosensitizing efficiency, and target specificity.[6,7]

In principle, when a PS possessing a significant σ_2 is excited by a femtosecond pulsed laser, a two-photon excitation process will readily take place where two lower-energy photons instead of one high-energy photon are simultaneously absorbed to excite the PS to its excited state (*i.e.*, PS*). Such an excitation mechanism opens up an avenue to the NIR excitation of PSs. It brings numerous benefits, including spatio-temporal resolution, diminished tissue autofluorescence, reduced photodamage, and deep tissue penetration.[33] From another perspective, the elevation of the production quantum yield of reactive oxygen species (ROS), particularly $^1O_2$, is an effective strategy to produce PS performance.[8,9] PSs with strong spin–orbital coupling (SOC) effect will prompt the conversion of short-lived singlet excited states to triplet excited states (*i.e.*, intersystem crossing, ISC) which enables energy transfer from ^{3}PS* to $^3O_2$, enhancing the Φ_Δ.[10–12]

Cyclometalated Ir(III) complexes demonstrate great versatility in photophysical properties, such as decent σ_2 in the NIR region, prominent Φ_Δ, *etc.*, and have been considered potential PS candidates by their peculiar accumulation patterns within cells. In addition to these unique merits, the properly designed architecture of Ir(III) complexes could elongate the excited state lifetime or introduce favorable mechanisms of

[a]*MOE Key Laboratory of Bioinorganic and Synthetic Chemistry, Guangdong Basic Research Center of Excellence for Functional Molecular Engineering, School of Chemistry, Sun Yat-Sen University, Guangzhou, 510275, P. R. China. E-mail: ceschh@mail.sysu.edu.cn*
[b]*The Institute of Flexible Electronics (IFE, Future Technologies), Xiamen University, Xiamen, 361102, P. R. China. E-mail: liujping@xmu.edu.cn*
[c]*Department of Dermatology, The East Division of the First Affiliated Hospital, Sun Yat-Sen University, Guangzhou, 510700, P. R. China. E-mail: cometvivi@126.com*
[d]*MOE Key Laboratory of Theoretical Organic Chemistry and Functional Molecule, School of Chemistry and Chemical Engineering, Hunan University of Science and Technology, Xiangtan, 400201, P. R. China*

†Electronic supplementary information (ESI) available. See DOI: https://doi.org/10.1039/d4dt01665c

‡These authors contributed equally to this work.

action to promote their PDT performance:[13,14] a type I PDT mechanism may emerge when the cyclometalated Ir(III) frameworks are conjugated with organic fluorophores, such as boron-dipyrromethene (BODIPY),[15] rhodamine,[9] or coumarin;[16] and extended excited state lifetimes of Ir(III) complexes may be achieved by the inclusion of isoenergetic or even low-lying pyrene groups to reshape the frontier orbitals of the complexes. However, in many cases, such bulky modifications are suspected of compromising biocompatibility and rendering the complexes unstable when excited, jeopardizing the catalytic renewal process of the PSs and thus entailing administration of a higher dose.[17] Hence, compact and robust structural modifications tailored to the fulfillment of full exploitation of cyclometalated Ir(III) PS* are in high demand.

1,2,4,5-Tetrazine is known as a small electron-deficient 4π compound containing an N=N double bond, which has been extensively utilized in the inverse electron-demanding Diels–Alder reactions for bioorthogonal chemistry. The conjugation of the tetrazine fragment with the cyclometalated Ir(III) moiety, which is electron-deficient, is very likely to strengthen the thermodynamic driving force in its reaction with dienophiles (which can be a "mini tag" of specific biomolecules), thus realizing the rapid ligation of Ir(III) PSs to the target of interest, especially cancer cells.[36] Such a design strategy endows the PSs with target specificity and alleviates concern about dose-associated adverse effects.

Aiming to fulfill the design of high-performance versatile Ir(III) PSs, here we covalently grafted the 1,2,4,5-tetrazine ring onto the dpip (1,2-diphenyl-1*H*-imidazo[4,5-*f*][1,10]phenanthroline) main ligand scaffold of Ir(III) matrices and synthesized three novel complexes (**Ir-ppy-Tz**, **Ir-pbt-Tz**, and **Ir-dfppy-Tz**, shown in Scheme 1) with varying cyclometalating auxiliary ligands (2-phenylpyridine, ppy; 2-phenylbenzo[*d*]thiazole, pbt; 2-(2,4-difluorophenyl)pyridine, dfppy) to further modulate their photophysical properties. Due to its highly electron-deficient nature, the tetrazine moiety probably dominates the contribution to the lowest-lying LUMO orbital in the newly formed cyclometalated Ir(III) complexes, which means photoinduced electron transfer to the tetrazine scaffold would occur. Combined with the fact that tetrazine has a mild radical nature and a strong triplet excited state oxidative potential,[18] such plausible electron transition would lead to two favorable results: (1) the tetrazine-based excited state lifetime is extended; (2) the PS* oxidizing ability is augmented and electron transfer from dpip-tetrazine^{*-} to biological intermediates is possible. Indeed, our *in vitro* experimental results validated the significant enhancement of Φ_Δ (by 40% for **Ir-pbt-Tz**) as well as the advent of a type I PDT mechanism for these well-thought-out PSs compared to the tetrazine-free counterparts and suggested very high PDT potency towards various cancer cell lines with IC_{50} values falling into the nanomolar regime. More in-depth investigations unveiled their promising TPA properties and mitochondria-targeted affinity.[19] These Ir(III) complexes exhibit strong two-photon PDT efficacy and represent a new series of potent PDT agents.

Results and discussion

Synthesis and characterization

The main ligand (*i.e.*, **dpip-Tz**) and chloro-bridged Ir(III) dimers were synthesized according to previously reported methods.[21,22] As shown in Fig. S1,† the Ir(III) complexes were synthesized by refluxing the dimers with **dpip-Tz**. The corresponding synthetic details are documented in the ESI.† The purified compounds are characterized with elemental analyses, HRMS, and ^{1}H, ^{13}C, and ^{19}F NMR spectroscopy (shown in Fig. S11–S20†).

As shown in Fig. 1, the Ir(III) complexes exhibit intense 250–325 nm absorptions and moderate absorptions around 400 nm with tails extending over 450 nm. The firm high-energy absorption peaks around 300 nm can be primarily assigned to intra-ligand charge transfer (ILCT). In contrast, the lower-energy absorption peaks around 400 nm can be assigned to a mixture of metal–ligand charge transfer (MLCT) and ligand–ligand charge transfer (LLCT). The dramatic absorption discrepancy of **Ir-pbt-Tz** with the other two above 400 nm gives

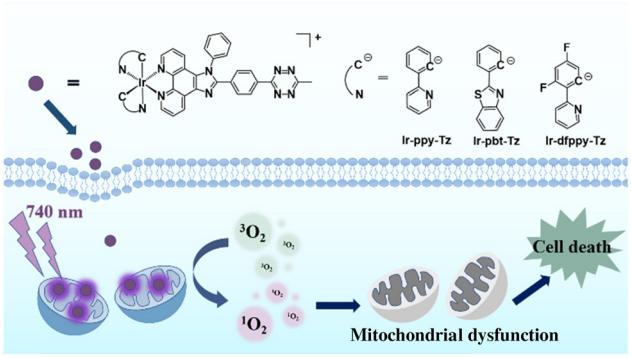

Scheme 1 Chemical structure and biological mechanism of the action of the Ir(III) complexes for two-photon PDT.

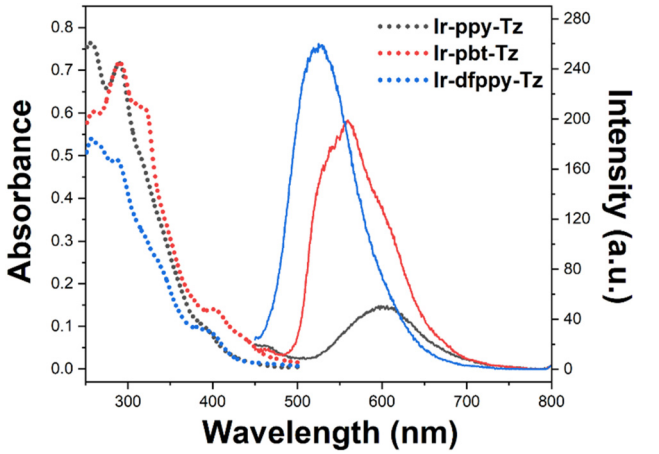

Fig. 1 UV-vis absorption (dotted line) and emission spectra (solid line) of **Ir-ppy-Tz**, **Ir-pbt-Tz** and **Ir-ppy-Tz** (10 μM) in methanol.

a hint of its reinforced LLCT oscillating strength and slightly elevated HOMO energy by the pbt auxiliary ligand. The photophysical properties of the complexes are summarized in Table S1.† Under ambient conditions and excitation at 405 nm, the complexes show different emission maxima (**Ir-ppy-Tz**: 600 nm, **Ir-pbt-Tz**: 559 nm, **Ir-dfppy-Tz**: 527 nm) with luminescent quantum yields ranging from 0.01 to 0.06. The lifetimes of these complexes span the range of 475–613 ns, which shows a dramatic elongation compared to conventional cyclometalated Ir(III) complexes. This phenomenon probably originates from the dpip-tetrazine^{*-} form that is more stabilized than other ordinary N^N ligand anion radicals in harboring the transitioning electron upon excitation. In addition, the emission intensity was attenuated when the oxygen levels increased (shown in Fig. S2†), indicating the triplet excited-state nature of these PSs*, which paves the way for the whole interaction of ^{3}PSs* with the ground state $^3O_2$.[23]

The two-photon absorption (TPA) cross-sections for **Ir-ppy-Tz**, **Ir-pbt-Tz**, and **Ir-dfppy-Tz** were determined using rhodamine B as a standard in an indirect method. The results are illustrated in Fig. S3a,† indicating that the highest σ_2 values for these complexes all emerge at 740 nm and were determined to be 44–102 GM (1 GM = 1 × 10^{-50} cm^4 s per photon per molecule). The two-photon excitation process was corroborated through a power-dependent emission intensity measurement where the emitted light is directly proportional to the square of the incident power (Fig. S3b†).

Numerous studies have explored the potential of bioorthogonal reactions, specifically tetrazine ligation, as a promising method for rapidly attaching photosensitizer agents to biomolecular targets to mitigate off-target side effects. However, experimental results (Fig. S4†) have not demonstrated this desired property in **Ir-pbt-Tz** under investigation. It is left to a future study to analyze such data. It is worth affirming that the PDT effect can be exerted by Ir(III) complexes modified with tetrazine functional groups at low concentrations.

ROS generation yield

For most PSs $^1O_2$ is the nexus between their photophysical properties and the PDT therapeutic outcome. In order to evaluate the Φ_Δ, different determination methods have been implemented. Electron spin resonance (ESR) associated with appropriate radical traps is a widely recognized method for detecting, identifying, and quantifying the ROS species produced by the photosensitized complexes. As shown in Fig. S5,† under irradiation (405 nm, 6 J cm^{-2}), the photogenerated $^1O_2$ oxidizes TEMP, yielding a paramagnetic TEMPO that gives strong three-line characteristic signals. Meanwhile, an appreciable amount of superoxide anions ($O_2^{\bullet-}$) was generated by using DMPO as the spin trap. These results suggest that the complexes undergo both type I and II PDT mechanisms, with the latter pathway being dominant, which aligns with our design expectation.

To further assess the capacity of the complexes to generate ROS under light, an indirect measurement that utilizes DPBF as the $^1O_2$ scavenger and Ru(bpy)$_3^{2+}$ (Φ_Δ = 0.81) as the standard compound was conducted. The oxidation of DPBF by photogenerated $^1O_2$ leads to a decrease in optical density at 411 nm in a stoichiometric manner and follows a zero-order kinetics process. Φ_Δ ($^1O_2$) values were calculated by comparison of the slope of the OD_{411} attenuation curve with the standard compound, as shown in Fig. S6 and Table S2.† The Φ_Δ values of both [Ir(ppy)$_2$(bpy)]$^+$ (0.35) and [Ir(ppy)$_2$(dpip)]$^+$ (0.40) were also determined, which indicate that Φ_Δ can be enhanced by extension of the main ligand conjugating system. A further comparison of Φ_Δ between [Ir(ppy)$_2$(dpip)]$^+$ and **Ir-ppy-Tz** verifies tetrazine's ability to promote photosensitization by a remarkable 40% enhancement. Amongst these complexes, **Ir-pbt-Tz** exhibits the most pronounced Φ_Δ (0.72), superior to the values for many commercial photosensitizers, including methylene blue (Φ_Δ = 0.52).[5]

Lipophilicity and intracellular distribution

The lipophilicity of a compound is closely associated with its physicochemical and physiological properties, especially cellular uptake and intracellular distribution. The lipid–water distribution coefficients ($\log P_{o/w}$) of the *n*-octanol/water system complexes were assessed, and the results are depicted in Fig. S7.† The indicated complexes show $\log P_{o/w}$ values within the +ve 0.4–0.8 range, suggesting a lipophilic cationic characteristic.[25] Among others, **Ir-pbt-Tz** exhibits the highest $\log P_{o/w}$ value, which may benefit its ability to cross the plasma membrane.[26]

A co-localization experiment with commercially available dyes was performed to study the intracellular distribution of the complexes. The perfect superimposition of the mitochondrial channel luminescent patterns (MitoTraker Deep Red FM) with the Ir(III) channel patterns explicitly demonstrates the mitochondria-targeted accumulation of these complexes with co-localization coefficients as high as 0.94 (**Ir-ppy-Tz**), 0.93 (**Ir-pbt-Tz**), and 0.90 (**Ir-dfppy-Tz**), respectively (Fig. 2). These findings align with previous reports regarding the mitochondria

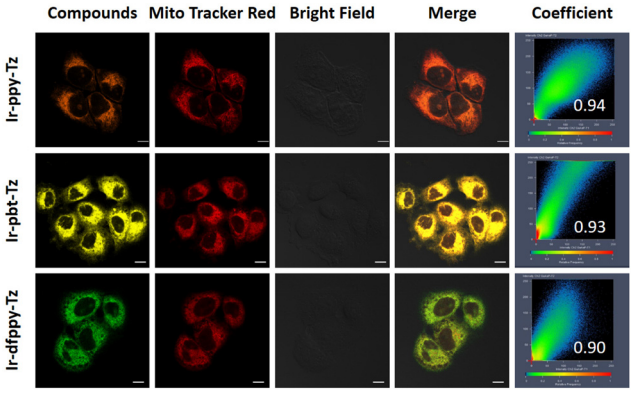

Fig. 2 CLSM imaging of A549 cells incubated with 1 μM Ir(III) complexes for 4 h at 37 °C (**Ir-ppy-Tz**: λ_{ex} = 405 nm, λ_{em} = 580–610 nm; **Ir-pbt-Tz**: λ_{ex} = 405 nm, λ_{em} =540–570 nm; **Ir-dfppy-Tz**: λ_{ex} = 405 nm, λ_{em} = 510–540 nm), followed by 50 nM of MitoTraker Deep Red (λ_{ex} = 633 nm, λ_{em} = 650–680 nm). Scale bar: 10 μm.

affinity of similar structures.[20,24,27,28] Mitochondria are double-membraned organelles that are responsible for various physiological and pathological processes, such as apoptosis, calcium regulation, and ROS management. Hence, mitochondria-targeted PDT can readily alter the redox balance by *in situ* ROS generation to overwhelm the cancer cells' survival ability.

Cytotoxicity assay

The (photo-)toxicities of the Ir(III) complexes in HLF primary lung fibroblast normal cells, as well as various cancer cell lines (A549 lung cancer cells, HeLa cervical cancer cells, and MDA-MB-231 breast cancer cells), were assessed using the MTT assay. The IC_{50} values under different conditions are summarized in Table 1. **Ir-pbt-Tz** outperformed others in phototoxicity in every cell line and exhibited a stunning IC_{50} (light) value of 24.0 nM towards A549 cells with a phototoxic index (PI) of 350, which is more potent than the values for most of the reported cyclometalated Ir(III) PSs.[26,27,29–31] In contrast, these complexes manifested relatively low dark toxicity (16.3–20.5 μM) to HLF cells. Indeed, the (photo-)toxicity to HLF normal cells was significantly reduced, which is favorable for alleviating unwanted photolesions to peripheral normal tissues. The ratio of the IC_{50} (light) of HLF to that of various cancer cell lines tested falls in the ranges of 3.5–4.3 (**Ir-ppy-Tz**), 2.7–5.7 (**Ir-pbt-Tz**), and 3.4–5.3 (**Ir-dfppy-Tz**), respectively. This phenomenon potentially stems from the enhanced uptake of cancerous cells compared to normal HLF cells because cancer cells' abnormally higher mitochondrial membrane potential can accumulate a more significant amount of lipophilic cationic PSs.[29] Based on this toxicity profile, A549 cells were selected to investigate further the mechanism of action involving the complex **Ir-pbt-Tz** in phototherapy.

ROS generation under two-photon excitation *in cellulo*

Since the complexes are TPA-active, they might provoke oxidative stress under NIR two-photon excitation. In order to evaluate the photogenerated ROS by the complex within cells, DCFH-DA was used as a fluorescent indicator. DCFH-DA can be readily internalized by viable cells, wherein it is enzymatically converted to ROS-sensitive non-emissive DCFH by esterase. Upon oxidation, DCFH is transformed into the non-membrane-permeable fluorescent compound 2,7-dichlorofluorescein (DCF). Hence, the fluorescence intensity of DCF can reflect the ROS level.[32] As shown in Fig. 3a, only when the

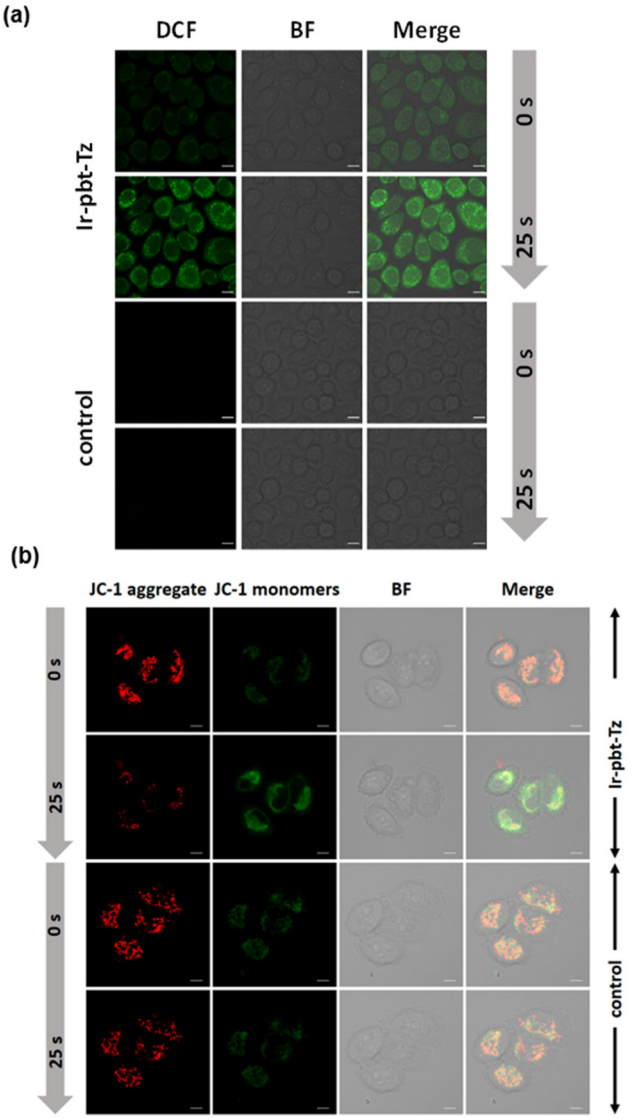

Fig. 3 (a) CLSM imaging of A549 cells incubated with the 1 μM DCFH-DA after pre-incubation with **Ir-pbt-Tz** (50 nM, 4 h, 37 °C) before and after two-photon PDT at 740 nm (6 J cm^{-2}). DCFH-DA: λ_{ex} = 488 nm, λ_{em} = 510–540 nm. Scale bar: 10 μm. (b) PDT effects on mitochondria membrane potentials induced by **Ir-pbt-Tz** (50 nM, 4 h, 37 °C). JC-1 aggregate: λ_{ex} = 543 nm, λ_{em} = 580–610 nm; JC-1 monomer: λ_{ex} = 488 nm, λ_{em} = 510–540 nm. Scale bar: 10 μm.

Table 1 (Photo)cytotoxicity (IC_{50}) of designed complexes towards different cell lines

	Ir-ppy-Tz		Ir-pbt-Tz		Ir-dfppy-Tz	
Cell lines	Light[a] (dark)	PI[b]	Light (dark)	PI	Light (dark)	PI
A549	96.0 nM (11.1 μM)	115	24.0 nM (8.4 μM)	350	58.3 nM (10.8 μM)	185
HeLa	119.5 nM (7.0 μM)	58	42.5 nM (6.4 μM)	151	84.1 nM (7.9 μM)	94
MDA-MB-231	100.1 nM (11.7 μM)	117	51.7 nM (8.1 μM)	156	89.9 nM (7.3 μM)	81
HLF	413.4 nM (20.5 μM)	50	137.4 nM (16.6 μM)	121	309.7 nM (16.3 μM)	53

[a] Irradiated using an LED area light source (405 nm, 6 J cm^{-2}). [b] PI = IC_{50} (dark)/IC_{50} (light).

treated cells were subject to a mild two-photon laser irradiation (740 nm, 6 J cm^{-2}), can the DCF green fluorescence signal be observed. In contrast, the control group lacking a **Ir-pbt-Tz** payload did not exhibit green fluorescence under either light or dark conditions. These results indicate that **Ir-pbt-Tz** can generate significant ROS under two-photon irradiation.

Mitochondrial membrane potential (MMP) assessment

Since mitochondria have been proved to be significant loci to accommodate the internalized Ir(III) complexes, mitochondrial dysfunction in post-PDT cells can be anticipated. MMP analysis provides a "canary in the coal mine" for the mitochondrial activity. JC-1, a commercial MMP dye, was used to evaluate the extent of mitochondrial damage caused.

JC-1 aggregates as a polymer (J-aggregates) in healthy mitochondria and emits red fluorescence in response to high mitochondrial membrane potential. In contrast, in dysfunctional or damaged mitochondria, a decrease in MMP leads to the release of JC-1 monomers into the cytosol, resulting in green fluorescence. As shown in Fig. 3b, after a mild two-photon PDT regimen (740 nm, 6 J cm^{-2}), cells treated with **Ir-pbt-Tz** exhibited a pronounced reduction in MMP, indicative of mitochondrial dysfunction. In contrast, the control group did not show any MMP changes even when receiving a two-photon PDT regimen.

Apoptosis analysis

Mitochondrial *in situ* photodamage prompts us to look closely at the mechanism of cell death, especially mitochondria-initiated apoptosis. A flow cytometry analysis on cells subjected to PDT using Annexin V-FITC/propidium iodide (PI) dual-staining was conducted. Annexin V-FITC is a phospholipid-binding protein that exhibits a high affinity for phosphatidylserine and detects early apoptotic cells by binding to exposed phosphatidylserine. Propidium iodide (PI) is a DNA dye that cannot cross intact cell membranes. However, in cells undergoing apoptosis or cell death, the increased membrane permeability allows PI to access DNA and emit red fluorescence, aiding in the identification of cells in the later stages of apoptosis or already deceased.

As depicted in Fig. S9,† most treated cells (more than 95%) were in the Q4 quadrant (AV^-/PI^-) under dark conditions. However, upon exposure to both irradiation and 25 nM **Ir-pbt-Tz**, the Q4 quadrant proportion decreased to 35.6%, while the proportions in the Q3 quadrant (AV^+/PI^-, 36.0%) and Q2 quadrant (AV^+/PI^+, 23.0%) increased. Increasing the incubation concentration to 50 nM, the Q4 quadrant proportion decreased to 10.1%, while the proportions of the Q3 quadrant (AV^+/PI^-, 36.2%) and the Q2 quadrant (AV^+/PI^+, 44.2%) increased more significantly. This suggests a transition of cell status from early to late apoptosis with an increased incubation concentration of **Ir-pbt-Tz** under irradiation. Meanwhile, this finding indicates that apoptosis is the predominant mode of cell death under PDT.

Following the application of two-photon PDT, cell viability was assessed using calcein AM (live)/EthD-1 (dead) dual staining. It was observed that upon irradiation (740 nm, 6 J cm^{-2}), the green fluorescence diminished, and there was a notable increase in dead cells exhibiting red fluorescence, specifically within the drugged group (Fig. 4). These findings suggest that the compound effectively kills tumor cells under two-photon irradiation.

Two-photon laser penetrating ability and ROS generation in 3D multicellular tumor spheroids (MCTS)

Compared to 2D cancer cell monolayers, A549 3D MCTS have been shown to replicate the tumor microenvironment's spatial heterogeneity better.[34] Confocal laser scanning microscopy (CLSM) along the *Z*-axis enables the visualization of complexes in sections at varying depths within the spheroids. As shown in Fig. 5a, two-photon excitation at 740 nm allows for a penetration depth of 146 μm, whereas one-photon excitation at 405 nm is limited to within the scope of 100 μm. This result highlights the advantage of two-photon PDT in achieving deeper tissue penetration.

The production of ROS by **Ir-pbt-Tz** within 3D MCTS was assessed using DCFH-DA. Following incubation with **Ir-pbt-Tz**, the absence of green fluorescence was noted under dark conditions; however, upon exposure to two-photon irradiation (740 nm, 6 J cm^{-2}), a prominent green fluorescence signal was observed. In contrast, the control group exhibited no fluo-

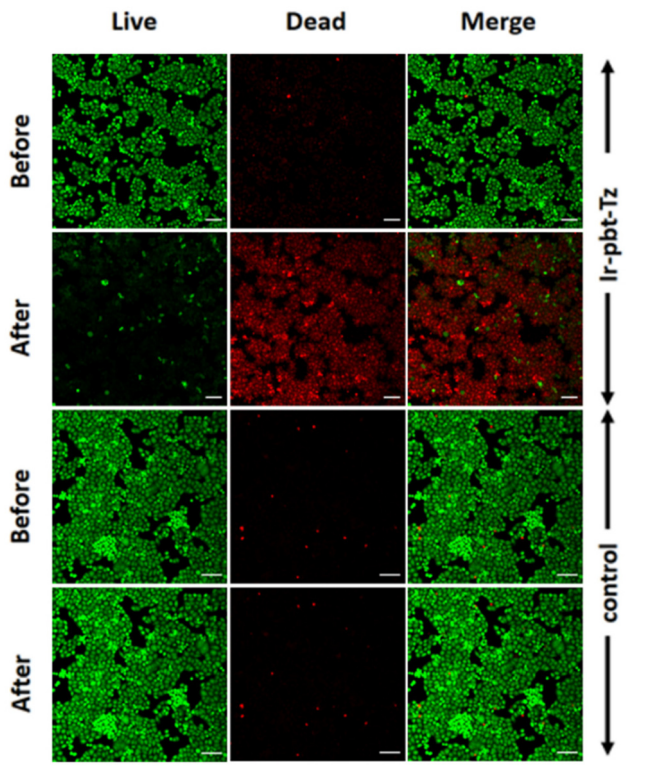

Fig. 4 Fluorescence microscopy images of A549 cells upon incubation with **Ir-pbt-Tz** (50 nM) for 4 h and calcein-AM (live cells, green, 0.5 μM, λ_{ex} = 488 nm, λ_{em} = 510–540 nm)/EthD-1 (dead cells, red, 2 μM, λ_{ex} = 530 nm, λ_{em} = 640–670 nm) in the dark or upon irradiation (740 nm, 6 J cm^{-2}). Scale bar: 100 μm.

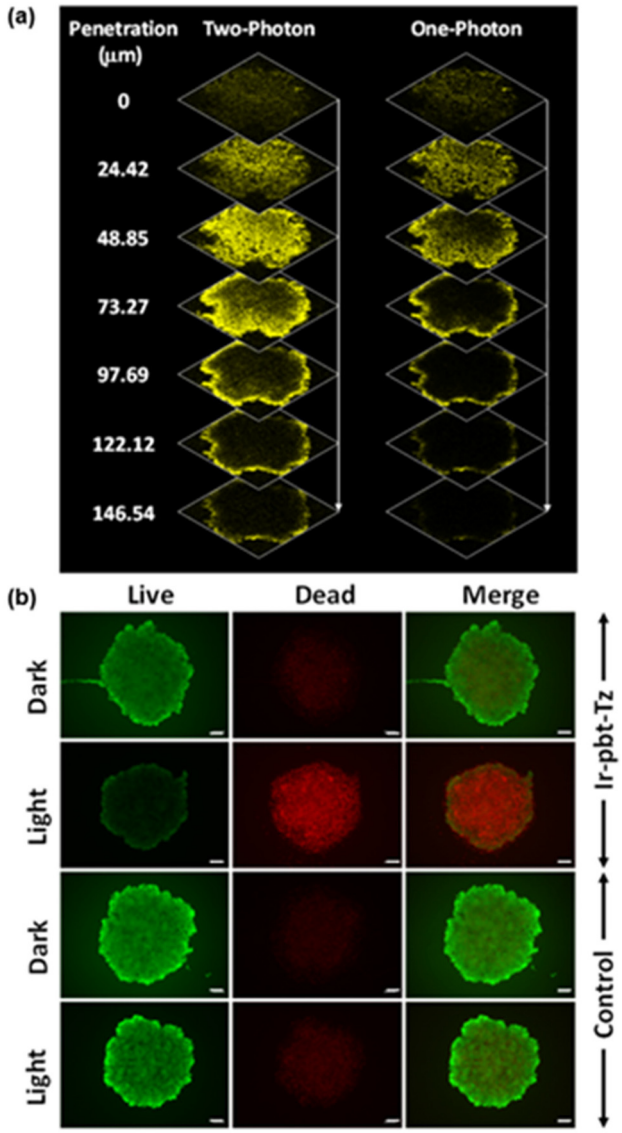

Fig. 5 (a) Penetration depth of **Ir-pbt-Tz** (1 μM, 4 h) in A549 3D MCTS under one- or two-photon irradiation. The excitation wavelengths of OPM and TPM were 405 and 740 nm, respectively. (b) Live/dead dual staining of the PDT effect of MCTS. The MCTS were incubated with 50 nM **Ir-pbt-Tz** for 4 h and then incubated with calcein AM (live cells, green, 0.5 μM, λ_{ex} = 488 nm, λ_{em} = 510–540 nm)/EthD-1 (dead cells, red, 2 μM, λ_{ex} = 530 nm, λ_{em} = 640–670 nm) in the dark or upon irradiation (740 nm, 6 J cm^{-2}).

rescence signal under either dark or two-photon irradiation conditions (Fig. S10†), indicating the photosensitizing ability of **Ir-pbt-Tz** under two-photon excitation in 3D MCTS.

Given **Ir-pbt-Tz**'s capacity to generate ROS *via* two-photon irradiation, its two-photon PDT potency was further assessed in 3D MCTS. The calcein AM/EthD-1 dual staining experiment was carried out on MCTS to visualize the live and dead cells. While green fluorescence of calcein AM in MCTS indicative of cell survival was evident in the absence of light input, the subsequent two-photon irradiation led to a divergent result (Fig. 5b). A549 MTCS preloaded with a **Ir-pbt-Tz** warhead showed a reduction of green fluorescence and a dramatic increase in red fluorescence of EthD-1 from dead cells. In contrast, no apparent changes were observed in the control group. This result suggests that **Ir-pbt-Tz** effectively induces cell death even in MCTS under a two-photon PDT regimen.

Conclusions

In this study, we designed, synthesized, and characterized a novel series of cyclometalated Ir(III) complexes with an electron-deficient tetrazine fragment covalently conjugated to the main ligand. Including tetrazine enables a more stabilized excited state of the complexes, resulting in a more $^1O_2$-productive type II PDT process and the advent of a type I mechanism. Amongst the complexes with varying auxiliary ligands, **Ir-pbt-Tz** was identified as a promising two-photon PS with the highest Φ_Δ (0.72) and σ_2 (102 GM). **Ir-pbt-Tz** targets mitochondria and the mediated PDT gives rise to mitochondrial MMP loss and, ultimately, cell apoptosis. The (photo-)toxicity profile of the newly synthesized complexes on various cancerous cell lines and HLF normal cell lines revealed that **Ir-pbt-Tz** exhibits the highest potency towards A549 lung cancer cells with an IC_{50} (light) value as low as 24 nM and a PI value as high as 350. Of note, this PI value is 5.7 times higher than that for the HLF normal cell line, implying its selective lethality between these cells. Finally, the two-photon PDT activity of **Ir-pbt-Tz** in 3D MCTS was fully validated by an array of MCTS experiments. All these results suggest that **Ir-pbt-Tz** is a promising PS candidate for two-photon PDT.

Experimental section

General information

Unless otherwise indicated, all chemicals are purchased from commercial sources and are of analytical reagent grade. The materials 1,10-phenanthroline-5,6-dione, 4-cyanobenzaldehyde, aniline, $Zn(OTf)_2$, $IrCl_3{\cdot}3H_2O$ were purchased from the Energy Chemical Company. 3-(4,5-Dimethylthiazol-2-yl)-2,5-diphenyltetrazolium bromide (MTT) was obtained from Sigma Aldrich Trading Co., Ltd (USA). The cell culture was performed in Dulbecco's Modified Eagle's medium (DMEM) with 1% penicillin/streptomycin and 10% fetal bovine (FBS) at 37 °C in 5% CO_2 and 95% air. DMEM, FBS, and penicillin/streptomycin were purchased from Gibco (USA). MitoTracker Deep Red and 2′,7′-dichlorofluorescein diacetate (DCFH-DA) were purchased from Thermo Fisher (USA). The annexin V-FITC apoptosis detection kit and the calcein/PI cell viability/cytotoxicity assay kit were purchased from Beyotime. All buffer components were of biological grade, obtained from commercial suppliers, and used as received.

Microanalyses (C, H, and N) were determined using an elemental analyzer (Elementar, Vario EL Cube). The HR-ESI-MS spectra were recorded on an LCQ system (Finnigan

MAT, USA). At room temperature, nuclear magnetic resonance (NMR) spectra were obtained on a Bruker AVANCE III 400 MHz NMR spectrometer. All chemical S4 shifts of the NMR spectra are given relative to tetramethylsilane (TMS). A PerkinElmer Lambda 950 spectrometer recorded the ultraviolet–visible (UV-vis) absorption spectra. Luminescence emission spectra were obtained on a Hitachi F-4500 luminescence spectrometer. The EPR measurements were determined using a Bruker model EMXPlus-10/12 spectrometer at 298 K. Inductively coupled plasma mass spectrometry (ICP-MS) experiments were conducted on an iCAP RQ (ThermoFisher) spectrometer. Confocal fluorescence imaging was conducted using an LSM-880 (Carl Zeiss Co., Ltd, Germany) laser scanning confocal microscope with an oil-immersion objective lens. Time-resolved emission and two-photon absorption cross-section measurements were performed on an SR-500I-D1 (femtosecond fluorescence spectrum measurement system, Coherent Inc.). Cell viability was measured using a SpectraMax CMax Plus (Molecular Devices) absorbance microplate reader.

Synthesis of ligand dpip-CN

The ligand **dpip-CN** was synthesized following the synthetic method reported in the literature: 1,10-phenanthroline-5,6-dione (0.84 g, 0.4 mmol), ammonium acetate (4.62 g, 60 mmol), 4-cyanobenzaldehyde (0.66 g, 5 mmol) and aniline (0.37 g, 4 mmol) were mixed in 50 mL of glacial acetic acid and refluxed at 120 °C. The crude product was purified using silica gel column chromatography (DCM/MeOH, v/v = 100 : 1), and the solvent was removed by rotary evaporation to obtain 1.46 g of yellow solid. Yield: 92%. ^{1}H NMR (400 MHz, chloroform-d$_3$) δ 9.24 (d, J = 4.1 Hz, 1H), 9.15 (d, J = 7.0 Hz, 1H), 9.09 (d, J = 3.0 Hz, 1H), 7.80 (dd, J = 8.1, 4.5 Hz, 1H), 7.73 (m, 5H), 7.61 (d, J = 8.4 Hz, 2H), 7.56 (d, J = 7.1 Hz, 2H), 7.45 (d, J = 8.4 Hz, 1H), 7.33 (dd, J = 8.4, 4.3 Hz, 1H). ^{13}C NMR (126 MHz, chloroform-d) δ 149.85, 148.79, 148.36, 144.24, 143.44, 137.39, 136.21, 133.97, 132.14, 131.36, 130.99, 129.50, 128.53, 128.34, 127.60, 123.95, 123.84, 122.62, 119.77, 118.26, 112.82. HR-ESI-MS (CH_3OH), calcd: m/z = 398.14002 $[M + H^+]^+$, found: 398.14039.

Synthesis of ligand dpip-Tz

The ligand **dpip-Tz** was synthesized according to the methods reported in the literature.[22] **Dpip-CN** (111 mg, 0.28 mmol), Zn(OTf)$_2$ (51.3 mg, 0.14 mmol), acetonitrile (0.15 mL, 2.8 mmol), 1,4-dioxane (10 mL), and hydrazine hydrate (0.44 mL, 14.0 mmol) were mixed under the argon and refluxed at 85 °C, and then the reaction was cooled to room temperature. 10 mL of $NaNO_2$ aqueous solution (38.6 mg, 5.60 mmol) was added to the reaction solution. The pH was adjusted to 3 with HCl. The crude products were purified by column chromatography on alumina using methanol/dichloromethane as the eluent. Yield: 38%. ^{1}H NMR (400 MHz, chloroform-d$_3$) δ 9.38 (s, 1H), 9.16 (d, J = 8.2 Hz, 2H), 8.56 (d, J = 5.9 Hz, 2H), 7.90–7.49 (m, 10H), 3.11 (s, 3H). ^{13}C NMR (126 MHz, DMSO-d$_6$) δ 167.64, 163.21, 152.20, 147.24, 137.21, 135.53, 133.25, 133.13, 131.58, 131.40, 130.45, 129.22, 127.79, 126.39, 125.30, 124.62, 120.70, 21.35. HR-ESI-MS (CH_3OH), calcd: m/z = 467.17272 $[M + H^+]^+$, found: 467.17284.

Synthesis of the complex Ir-ppy-Tz

The ligand **dpip-Tz** (93.2 mg, 0.2 mmol) and the cyclometalated dichloro-bridged dimers $[Ir_2(ppy)_4(\mu\text{-}Cl)_2]$ (0.1 mmol) were mixed in methanol/dichloromethane (1 : 1, v/v, 20 mL) and refluxed at 65 °C for 6 h under an argon atmosphere. After the reaction, the mixture was allowed to cool naturally to room temperature, and the solvent was removed by rotary evaporation. The elution was carried out with a 100 : 1 (v/v) mixed solvent combination (methanol : dichloromethane). The yield, HR-ESI-MS, and ^{1}H/^{19}F/^{13}C NMR results are as follows: yield 74.2 mg, 74%. ^{1}H NMR (400 MHz, methanol-d$_4$) δ 9.37 (d, J = 8.3 Hz, 1H), 8.48 (d, J = 8.2 Hz, 2H), 8.39 (d, J = 4.8 Hz, 1H), 8.26 (d, J = 4.8 Hz, 1H), 8.18–8.09 (m, 2H), 8.05–7.98 (m, 1H), 7.89 (d, J = 8.2 Hz, 2H), 7.75 (t, J = 30.7, 15.4, 8.2 Hz, 8H), 7.54 (dd, J = 15.9, 5.0 Hz, 3H), 7.19 (d, J = 7.3 Hz, 1H), 7.14 (d, J = 7.4 Hz, 1H), 7.11–7.05 (m, 2H), 6.93 (t, J = 8.2 Hz, 4H), 6.41 (t, J = 8.1 Hz, 2H), 3.01 (s, 3H). ^{13}C NMR (126 MHz, DMSO-d$_6$) δ 167.71, 167.32, 163.23, 153.24, 150.94, 150.53, 149.98, 149.88, 149.59, 148.97, 145.29, 144.85, 144.44, 139.23, 136.88, 136.70, 133.56, 132.96, 131.75, 131.66, 131.40, 130.75, 130.61, 130.26, 129.24, 128.56, 128.36, 127.91, 127.10, 126.52, 125.58, 124.37, 124.29, 122.89, 122.54, 120.49, 21.36. HR-ESI-MS (CH_3OH), calcd: m/z = 967.25917 $[M - Cl^-]^+$; found: 967.25642. calcd for $C_{50}H_{34}N_{10}ClIr$ (%): C, 59.90; H, 3.42; N, 13.97. Found (%): C, 59.73; H, 3.73; N, 13.85.

Synthesis of the complex Ir-pbt-Tz

As mentioned above, other procedures were similar to that for **Ir-ppy-Tz**, using $[Ir_2(pbt)_4(\mu\text{-}Cl)_2]$ instead of $[Ir_2(ppy)_4(\mu\text{-}Cl)_2]$. Yield 75.8 mg, 69%. ^{1}H NMR (400 MHz, methanol-d$_4$) δ 9.45 (d, J = 8.3 Hz, 1H), 8.60 (d, J = 5.0 Hz, 1H), 8.47 (d, J = 4.9 Hz, 1H), 8.42 (d, J = 8.4 Hz, 2H), 8.15 (dd, J = 8.3, 5.1 Hz, 1H), 8.03–7.94 (m, 4H), 7.85 (d, J = 8.3 Hz, 3H), 7.80–7.75 (m, 3H), 7.70 (dd, J = 8.7, 5.0 Hz, 2H), 7.58 (d, J = 8.5 Hz, 1H), 7.29 (m, 2H), 7.22–7.15 (m, 2H), 6.99–6.89 (m, 4H), 6.52 (dd, J = 7.5, 2.7 Hz, 2H), 5.99 (t, J = 8.2 Hz, 2H), 3.04 (s, 3H). ^{13}C NMR (126 MHz, DMSO-d$_6$) δ 181.85, 181.79, 167.68, 163.22, 153.63, 140.61, 136.78, 136.36, 133.54, 133.26, 132.95, 132.59, 131.72, 131.68, 131.60, 131.36, 131.24, 130.66, 129.29, 128.64, 128.33, 127.84, 127.57, 127.43, 126.40, 126.33, 126.11, 125.10, 116.98, 21.35. HR-ESI-MS (CH_3OH), calcd: m/z = 1079.20331 $[M - Cl^-]^+$; found: 1079.19653. Calcd for $C_{54}H_{34}N_{10}S_2ClIr$ (%): C, 58.18; H, 3.07; N, 12.57. Found (%): C, 58.06; H, 3.32; N, 12.49.

Synthesis of the complex Ir-dfppy-Tz

This compound was synthesized according to the same procedure as that for **Ir-ppy-Tz**, using $[Ir_2(dfppy)_4(\mu\text{-}Cl)_2]$ instead of $[Ir_2(ppy)_4(\mu\text{-}Cl)_2]$. Yield 83.9 mg, 78%. ^{1}H NMR (500 MHz, DMSO-d$_6$) δ 9.39 (dd, J = 8.3, 1.3 Hz, 1H), 8.47 (d, J = 8.5 Hz, 2H), 8.38–8.26 (m, 3H), 8.22–8.15 (m, 2H), 7.99 (m, 2H), 7.88 (d, J = 8.6 Hz, 2H), 7.85 (d, J = 8.0 Hz, 2H), 7.83–7.73 (m, 4H), 7.60 (d, J = 8.5 Hz, 1H), 7.59–7.54 (m, 2H), 7.14–7.07 (m, 2H), 7.05–6.95 (m, 2H), 5.71 (m, 2H), 3.00 (s, 3H). ^{19}F NMR

(376 MHz, methanol-d_4) δ −108.02 (dd, J = 10.6, 7.2 Hz), −110.47 (d, J = 10.8 Hz). ^{13}C NMR (126 MHz, DMSO-d_6) δ 167.71, 164.27, 163.23, 162.28, 160.12, 155.00, 154.64, 153.35, 150.44, 150.32, 149.63, 144.93, 144.52, 140.48, 136.80, 136.76, 133.60, 133.52, 132.93, 131.81, 131.44, 130.83, 130.63, 129.22, 128.65, 128.58, 128.24, 127.92, 127.48, 126.59, 124.96, 122.61, 113.93, 113.79, 99.65, 21.36. HR-ESI-MS (CH_3OH), calcd: m/z = 1039.22148 $[M - Cl^-]^+$; found: 1039.21480. Calcd for $C_{50}H_{30}N_{10}F_4ClIr$ (%): C, 55.89; H, 2.81; N, 13.04. Found (%): C, 55.73; H, 3.02; N, 12.88.

Log *P* measurement

The lipid–water distribution coefficient ($\log P_{O/W}$) is often used to judge the hydrophilicity or lipophilicity of compounds, which is determined by the standard "shake-flask" method. The *n*-octanol/water partition coefficient ($\log P$), is calculated using the following eqn (1):

$$\log P = \log(C_{[\text{solute}]\text{octanol}}/C_{[\text{solute}]\text{water}}) \quad (1)$$

The $[\text{solute}]_{\text{octanol}}$ and $[\text{solute}]_{\text{water}}$ were determined by UV absorption. The same volumes of *n*-octanol and water were mixed in a centrifuge tube, and the mixture was shaken at 37 °C in a shaker incubator overnight. The mixture was left to stir for 24 h and then allowed to stand for stratification. The upper layer was an *n*-octanol solution of saturated water, and the lower layer was an aqueous solution of saturated *n*-octanol. The two solutions were carefully separated, and the complex (5 μM) was dissolved in the *n*-octanol solution of saturated water. Then, the same volume of saturated *n*-octanol aqueous solution was added, and the mixture was shaken overnight, and the mixture was left to stir for 24 h. The aqueous and organic phases were separated, and the two phases were assayed at 290 nm wavelength with a UV/vis spectrophotometer, namely $[\text{solute}]_{\text{Octanol}}$ and $[\text{solute}]_{\text{Water}}$. The experimental group was paralleled three times.

Electron spin resonance (ESR) assay

The EPR measurements were carried out with a Bruker Model EMXPlus-10/12 spectrometer at 298 K. TEMP was used for trapping $^1O_2$, The concentration of TEMP was 25 mM, and then the TEMP was mixed with Ir(III) complexes, followed by irradiation (405 nm, 6 J cm^{-2}). The samples were promptly tested. DMPO (50 mM) was utilized as $^{\bullet}OH$ and $O_2^{\bullet-}$trap.

Two-photon absorption cross-section measurements

The two-photon absorption cross-section measurements were determined using the method established by Webb and Xu.[35] The two-photon luminescence of Ir(III) complexes (300 μL, 1.0 mM) in methanol through quartz cuvettes was collected by irradiation using a picosecond pulsed laser (690–800 nm). Two-photon absorption cross-section measurements (σ) were calculated using the following equation, while rhodamine B in methanol was used as a calibration standard:

$$\sigma_s = (\sigma_r \Phi_r c_r I_s n_s)/(\Phi_s c_s I_r n_r)$$

where σ is the TPA cross-section, Φ is the quantum yield, C is the concentration, n is the refractive index, and I is the integrated photoluminescent spectrum. The subscripts s and r represent sample and reference, respectively.

Singlet oxygen detection

The singlet oxygen yield of the complex was determined using an indirect method with the use of UV-vis spectroscopy. 1,3-Diphenylisobenzofuran (DPBF) was used as the $^1O_2$ detection probe, while $[Ru(bpy)_3]^{2+}$ was used as the standard. The absorbance of the complex at 405 nm was adjusted to the same value of 0.25 and then mixed with DPBF (60 μM) in methanol in quartz cuvettes. The above solution was irradiated with 405 nm light (10.9 mW cm^{-2}) every 2 s, and the absorbance at 411 nm was measured. The Φ_Δ was determined using the following equations:

$$\Phi_\Delta{}^s = \Phi_\Delta^r \times (s^s \times F^r)/(s^r \times F^s)$$
$$F = (1 - \text{OD}_{405}^s)/(1 - \text{OD}_{405}^r)$$

where Φ_Δ is the singlet oxygen yield, s is the decay rate of $\text{OD}_{405\ \text{nm}}$ with illumination time, F is the absorption correction factor, and superscripts r and s indicate sample and standard compounds, respectively.

Cell culture

The lung carcinoma A549 cell lines, the HeLa human cervix carcinoma cell line, the human triple-negative MDA-MB-231 breast cancer cells, and the human lung fibroblasts (HLFs) were all obtained from the American-Type Culture Collection (ATCC). The cells were cultured in DMEM media containing 10% fetal bovine serum (FBS), 100 units per ml penicillin and 50 μg ml^{-1} streptomycin. The culture conditions for all cells were 37 °C, 5% CO_2, and 95% humidity. The cells were passaged by successive trypsinization and re-seeding.

Monolayer cell cytotoxicity tests

Cytotoxicity was evaluated using the MTT assay. The cell lines were seeded in 96-well plates and incubated for 24 h. The Ir(III) complexes at various concentrations (1% DMSO) were added to the plates for adherent cell lines and then were incubated for another 4 h followed by replacement of the medium. The light group cells were irradiated with a lamp with a bandpass of 405 nm for 300 seconds (20 mW cm^{-2}), while the dark group cells without treatment were incubated for another 48 h. After that, 15 μL of MTT (5 mg mL^{-1}) was added to each well, and the cells were incubated for a further 4 h at 37 °C. The medium was aspirated and replaced with 150 μL per well of DMSO. After shaking for 2 min, the $\text{OD}_{595\ \text{nm}}$ values were measured with SpectraMax CMax Plus, Molecular Devices. The experimental group was analysed in parallel three times.

Cellular localization

An overnight culture of A549 cells (1×10^5 cells per mL) was prepared in Corning confocal dishes at 37 °C. After treatment with the complexes (1.0 μM) for 4 h, the cells were washed

with PBS and stained with MitoTracker Deep Red (50 nM) for 30 minutes. The cells were washed with PBS to remove the surplus dye. Then, the cells were imaged by confocal luminescence microscopy (Zeiss LSM 880 laser microscopy system).

ROS level detection

The DCFH-DA assay was used to measure intracellular ROS production by complexes under two-photon excitation. The A549 cells were seeded in a confocal laser dish at a density of 1×10^5 cells per mL and then were incubated with the complex (50 nM) for 4 h. Then the culture medium was refreshed, and the cells were incubated with the fluorescent probe DCFH-DA (1 μM) for 20 minutes. The light group was irradiated with two-photon irradiation (6 J, 5 min), while the dark group remained untreated. Fluorescent images were captured using an excitation wavelength of 488 nm, and the emission was recorded between 510 and 540 nm. The production of ROS was assessed using the same protocol in 3D multicellular spheroids.

Mitochondrial membrane potential detection

The A549 cells were seeded in a confocal laser dish at a density of 1×10^5 cells per mL and then were incubated with the complex (50 nM) for 4 h. Then the culture medium was refreshed, and the cells were incubated with JC-1 following the instructions. The samples were imaged using a confocal laser scanning microscope. Fluorescent images of the JC-1 aggregate were captured using an excitation wavelength of 543 nm. The emission was recorded in the range of 580–610 nm, while images were acquired using an excitation wavelength of 488 nm, and the emission was recorded between 510 and 540 nm for the JC-1 monomer. The light groups were exposed to two-photon irradiation (740 nm, 6 J cm^{-2}) and then incubated for 20 minutes. The light group samples were photographed under a confocal microscope. Photographs were taken under the same conditions. Controls were managed under the same conditions as for the experimental group except for the incubation of Ir(III) complexes.

Annexin V-FITC/propidium iodide (AV/PI)

A549 cells were seeded into 6-well plates at 1×10^5 cells per well density and incubated with different concentrations of complexes (0.25 nM and 50 nM) for 4 h. The culture medium was refreshed, and the cells were irradiated (405 nm, 20 mW cm^{-2}) for 300 s or kept in the dark. The experimental operation was conducted according to the annexin V-FITC kit instructions and the samples were analyzed using flow cytometry.

Live/dead viability assay

A549 cells were seeded into 96-well plates at 1×10^4 cells per well density incubated with complexes (50 nM) for 4 h. The culture medium was refreshed, and then calcein AM and ethidium homodimer-1 (EthD-1) were added according to the instructions. After further incubation, cells were photographed with a confocal microscope. In the dark groups, fluorescent images of calcein-AM were acquired using an excitation wavelength of 488 nm. The emission was recorded in the range of 510–540 nm, while images were acquired using an excitation wavelength at 530 nm, and the emission was recorded between 640 and 670 nm for EthD-1. In the light groups, the cells were exposed to two-photon irradiation (740 nm, 6 J cm^{-2}) and photographed under the same conditions. Controls were managed under the same conditions as for the experimental group except for the incubation of Ir(III) complexes. The same protocol was used for 3D multicellular spheroids.

Z-Axis scanning of 3D MCSs

The culture of 3D multicellular spheroids was prepared following a previously reported method. A suspension of 1.5% agarose in fresh PBS and A549 cells was added to a 96-well microassay culture plate until the total volume was 200 μL per well. The form of A549 3D MCSs with an average diameter of 800 μm was cultured in a 37 °C incubator for 3 days. At the same time, the culture medium was replaced every two days. A549 3D MCSs were incubated with Ir(III) complexes (1 μM, 1% DMSO) for 4 h. Then the cells were imaged using a confocal microscope. For one-photon imaging, the excitation wavelength was 405 nm, while it was 740 nm for two-photon imaging.

Data availability

The data supporting this article have been included as part of the ESI.†

Conflicts of interest

There are no conflicts to declare.

Acknowledgements

This work was supported by the National Natural Science Foundation of China (No. 22120102002 and 92353301) and the Science and Technology Innovation Program of Hunan Province of China (No. 2021RC5028). J. Liu thanks the Academy of Medical Sciences Newton International Fellowship for funding through NIFR7/1063.

References

1 P. Agostinis, K. Berg, K. A. Cengel, T. H. Foster, A. W. Girotti, S. O. Gollnick, S. M. Hahn, M. R. Hamblin, A. Juzeniene, D. Kessel, M. Korbelik, J. Moan, P. Mroz, D. Nowis, J. Piette, B. C. Wilson and J. Golab, *Ca-Cancer J. Clin.*, 2011, **61**, 250–281.
2 X. Zhao, J. Liu, J. Fan, H. Chao and X. Peng, *Chem. Soc. Rev.*, 2021, **50**, 4185–4219.
3 X. Li, S. Lee and J. Yoon, *Chem. Soc. Rev.*, 2018, **47**, 1174–1188.

4 K. Yamagishi, I. Kirino, I. Takahashi, H. Amano, S. Takeoka, Y. Morimoto and T. Fujie, *Nat. Biomed. Eng.*, 2019, **3**, 27–36.
5 J. Liu, Y. Chen, G. Li, P. Zhang, C. Jin, L. Zeng, L. Ji and H. Chao, *Biomaterials*, 2015, **56**, 140–153.
6 Z. Zhou, J. Liu, T. W. Rees, H. Wang, X. Li, H. Chao and P. J. Stang, *Proc. Natl. Acad. Sci. U. S. A.*, 2018, **115**, 5664–5669.
7 Z. Zhou, J. Liu, J. Huang, T. W. Rees, Y. Wang, H. Wang, X. Li, H. Chao and P. J. Stang, *Proc. Natl. Acad. Sci. U. S. A.*, 2019, **116**, 20296–20302.
8 X. Miao, W. Hu, T. He, H. Tao, Q. Wang, R. Chen, L. Jin, H. Zhao, X. Lu, Q. Fan and W. Huang, *Chem. Sci.*, 2019, **10**, 3096–3102.
9 L. Zhou, F. Wei, J. Xiang, H. Li, C. Li, P. Zhang, C. Liu, P. Gong, L. Cai and K. Wong, *Chem. Sci.*, 2020, **11**, 12212–12220.
10 Z. Wang, L. Huang, Y. Yan, A. M. El-Zohry, A. Toffoletti, J. Zhao, A. Barbon, B. Dick, O. F. Mohammed and G. Han, *Angew. Chem., Int. Ed.*, 2020, **59**, 16114–16121.
11 K. Teng, W. Chen, L. Niu, W. Fang, G. Cui and Q. Yang, *Angew. Chem., Int. Ed.*, 2021, **60**, 19912–19920.
12 F. Monti, A. Baschieri, L. Sambri and N. Armaroli, *Acc. Chem. Res.*, 2021, **54**, 1492–1505.
13 P. Ho, C. Ho and W. Wong, *Coord. Chem. Rev.*, 2020, **413**, 213267.
14 C. Caporale and M. Massi, *Coord. Chem. Rev.*, 2018, **363**, 71–91.
15 L. Qiao, J. Liu, S. Kuang, X. Liao, J. Kou, L. Ji and H. Chao, *Dalton Trans.*, 2021, **50**, 14332–14341.
16 V. Novohradsky, A. Rovira, C. Hally, A. Galindo, G. Vigueras, A. Gandioso, M. Svitelova, R. Bresolí-Obach, H. Kostrhunova, L. Markova, J. Kasparkova, S. Nonell, J. Ruiz, V. Brabec and V. Marchán, *Angew. Chem., Int. Ed.*, 2019, **58**, 6311–6315.
17 L. Wang, S. Monro, P. Cui, H. Yin, B. Liu, C. G. Cameron, W. Xu, M. Hetu, A. Fuller, S. Kilina, S. A. McFarland and W. Sun, *ACS Appl. Mater. Interfaces*, 2019, **11**, 3629–3644.
18 J. Yuasa and S. Fukuzumi, *J. Am. Chem. Soc.*, 2006, **128**, 14281–14292.
19 A. Colombo, C. Dragonetti, V. Guerchais, C. Hierlinger, E. Zysman-Colman and D. Roberto, *Coord. Chem. Rev.*, 2020, **414**, 213293.
20 Y. Chen, T. W. Rees, L. Ji and H. Chao, *Curr. Opin. Chem. Biol.*, 2018, **43**, 51–57.
21 G. Li, Y. Chen, J. Wang, J. Wu, G. Gasser, L. Ji and H. Chao, *Biomaterials*, 2015, **63**, 128–136.
22 J. C. Carlson, L. G. Meimetis, S. A. Hilderbrand and R. Weissleder, *Angew. Chem., Int. Ed.*, 2013, **52**, 6917–6920.
23 P. Zhang, C. K. C. Chiu, H. Huang, Y. P. Y. Lam, A. Habtemariam, T. Malcomson, M. J. Paterson, G. J. Clarkson, P. B. O'Connor, H. Chao and P. J. Sadler, *Angew. Chem., Int. Ed.*, 2017, **56**, 14898–14902.
24 C. Jin, F. Liang, J. Wang, L. Wang, J. Liu, X. Liao, T. W. Rees, B. Yuan, H. Wang, Y. Shen, Z. Pei, L. Ji and H. Chao, *Angew. Chem., Int. Ed.*, 2020, **59**, 15987–15991.
25 K. Xiong, C. Qian, Y. Yuan, L. Wei, X. Liao, L. He, T. W. Rees, Y. Chen, J. Wan, L. Ji and H. Chao, *Angew. Chem., Int. Ed.*, 2020, **59**, 16631–16637.
26 J. Liu, C. Jin, B. Yuan, Y. Chen, X. Liu, L. Ji and H. Chao, *Chem. Commun.*, 2017, **53**, 9878–9881.
27 H. Yuan, Z. Han, Y. Chen, F. Qi, H. Fang, Z. Guo, S. Zhang and W. He, *Angew. Chem., Int. Ed.*, 2021, **60**, 8174–8181.
28 H. Huang, S. Banerjee, K. Qiu, P. Zhang, O. Blacque, T. Malcomson, M. J. Paterson, G. J. Clarkson, M. Staniforth, V. G. Stavros, G. Gasser, H. Chao and P. J. Sadler, *Nat. Chem.*, 2019, **11**, 1041–1048.
29 J. Liu, C. Jin, B. Yuan, X. Liu, Y. Chen, L. Ji and H. Chao, *Chem. Commun.*, 2017, **53**, 2052–2055.
30 J. S. Nam, M.-G. Kang, J. Kang, S.-Y. Park, S. J. C. Lee, H.-T. Kim, J. K. Seo, O.-H. Kwon, M. H. Lim, H.-W. Rhee and T.-H. Kwon, *J. Am. Chem. Soc.*, 2016, **138**, 10968–10977.
31 L. He, Y. Li, C. Tan, R. Ye, M. Chen, J. Cao, L. Ji and Z. Mao, *Chem. Sci.*, 2015, **6**, 5409–5418.
32 D. Yu, Y. Zha, Z. Zhong, Y. Ruan, Z. Li, L. Sun and S. Hou, *Sens. Actuators, B*, 2021, **339**, 129878.
33 Y. Chen, R. Guan, C. Zhang, J. Huang, L. Ji and H. Chao, *Coord. Chem. Rev.*, 2016, **310**, 16–40.
34 C. Fischbach, R. Chen, T. Matsumoto, T. Schmelzle, J. S. Brugge, P. J. Polverini and D. J. Mooney, *Nat. Methods*, 2007, **4**, 855–860.
35 C. Xu and W. W. Webb, *J. Opt. Soc. Am. B*, 1996, **13**, 481–491.
36 H. Wu and N. K. Devaraj, *Acc. Chem. Res.*, 2018, **51**, 1249–1259.